Applied Catalysis B: Environmental 302 (2022) 120868

Contents lists available at ScienceDirect

Applied Catalysis B: Environmental

journal homepage: www.elsevier.com/locate/apcatb

New insights into the efficient charge transfer of the modified-TiO_2/Ag_3PO_4 composite for enhanced photocatalytic destruction of algal cells under visible light

Li Zhou [a,b], Xu Zhang [a,b], Min Cai [a,b], Naxin Cui [a,b], Guifa Chen [a,b], Guoyan Zou [a,b,*]

[a] Eco-Environmental Protection Research Institute, Shanghai Academy of Agricultural Sciences, Shanghai 201403, China
[b] Shanghai Engineering Research Centre of Low-Carbon Agriculture, Shanghai 201403, China

ARTICLE INFO

Keywords:
b-N-TiO_2/Ag_3PO_4
Defects
Heterojunction
Band structure
Algal cells

ABSTRACT

A novel p-n heterojunction between Ag_3PO_4 and nitrogen-doped black TiO_2 (b-N-TiO_2) was successfully synthesized via the calcination and precipitation method. The incorporated nitrogen and produced oxygen vacancies in b-N-TiO_2 narrowed the bandgap and shifted the band position of TiO_2, which promoted p-n heterojunction formation and subsequently facilitated the separation of photogenerated electrons and holes in the composite b-N-TiO_2/Ag_3PO_4. The b-N-TiO_2/Ag_3PO_4 exhibited enhanced photocatalytic activity for chlorophyll-a degradation in *Microcystis aeruginosa* cells, which was 2.73, 7.72, and 6.04 times higher than that of the pure Ag_3PO_4, b-N-TiO_2, and P25/Ag_3PO_4, respectively. Furthermore, the mechanism exploration indicated the transfer pathways of photo-produced electrons and holes to generate the dominant superoxide anion radicals ($\bullet O_2^-$) in photocatalytic processes. The charge transfer increased the photocatalytic stability of the composite b-N-TiO_2/Ag_3PO_4 compared with pure Ag_3PO_4 and P25/Ag_3PO_4. This research provides a new perspective into the roles of defects to form heterojunctions in photocatalytic composites.

1. Introduction

Because of water eutrophication and global warming, harmful algal blooms (HABs) have been one of the most serious disasters in the environment, as they cause immense damage to the aquatic ecosystem [1]. To address cyanobacteria blooms, many physical and chemical methods have been developed, such as manual mechanical salvage and $CuSO_4$ dosage [2]. However, applications of these traditional methods have been limited due to high costs or secondary pollution. Photocatalytic degradation of contaminants using inexhaustible solar is one of the most promising methods to counter the HABs problem, as visible-light-induced photocatalysts have drawn great attention for environmental remediation [3]. Wang et al. reported N, P co-doped TiO_2/expanded graphite carbon layer composite, which presented a removal rate of 98.15% for *Microcystis aeruginosa* cells after 9 h visible light irradiation [4]. The composite Ca-Ag_3PO_4 exhibited above 96% removal rate for nannochloropsis oculata after 12 h visible light irradiation [5]. The photocatalytic technology has been gradually applied in HABs control in recent years.

Recently, Ag_3PO_4 has been used for the abatement of HABs as a kind of visible-light-driven photocatalyst. Although Ag_3PO_4 is an attractive material because of its 90% high quantum efficiency under the light ($\lambda > 420$ nm) irradiation [6], the reducing capacity of photo-generated electrons accumulating on Ag_3PO_4 conduction band (CB) is weak because of the positive CB level. Moreover, electrons on the CB of Ag_3PO_4 could combine with the Ag^+ to form deposited Ag^0 on the Ag_3PO_4 surface, which is the adverse factor for its photocatalytic activity and stability during water treatment application [7]. Therefore, utilizing the photo-induced electrons on the CB of the Ag_3PO_4 is key to improving the photoactivity and stability of visible-light-induced Ag_3PO_4. The formation of heterojunction has been used to overcome the above-mentioned disadvantages of Ag_3PO_4-based composite photocatalysts [8]. TiO_2 is one of the most common photocatalysts due to its excellent photocatalytic properties and excellent characteristics [9]. According to the band structures of TiO_2 and Ag_3PO_4, TiO_2 and Ag_3PO_4 can form a well-matched heterojunction structure [10]. There have been reports of Ag_3PO_4-TiO_2 heterojunction for pollutant degradation [11–15]. Liu et al. determined the electronic band structures of TiO_2 and Ag_3PO_4 and demonstrated that the Ag_3PO_4-TiO_2 type II heterojunction could enhance the evolution of photocatalytic hydrogen [16]. However,

* Corresponding author at: Eco-Environmental Protection Research Institute, Shanghai Academy of Agricultural Sciences, Shanghai 201403, China.
E-mail address: zouguoyan@263.net (G. Zou).

https://doi.org/10.1016/j.apcatb.2021.120868
Received 25 August 2021; Received in revised form 9 October 2021; Accepted 27 October 2021
Available online 30 October 2021

the proposed mechanisms of charge transfer and enhanced photocatalytic activity remain contradictory. On the one hand, it is difficult to transfer electrons from CB of Ag_3PO_4 (+0.45 eV (vs. NHE)) to oxygen molecules to form $\bullet O_2^-$ (−0.284 V (vs. NHE)). However, in some studies of the Ag_3PO_4-TiO_2 system, $\bullet O_2^-$ was the dominant oxidative species [15]. In other aspects, the heterojunction formation between TiO_2 and Ag_3PO_4 not only enhanced the separation of photo-induced electrons and holes but also improved the Ag_3PO_4 structural stability. However, in the TiO_2-Ag_3PO_4 system, the accumulated photo-induced electrons in the CB of the Ag_3PO_4 did not transfer to inhibit the reduction of Ag^+. In some studies, the improved structural stability was ascribed to the re-transport of holes on TiO_2 to the Ag_3PO_4, thus leading to the re-oxidation of Ag^0 to Ag^+. However, no direct evidence exists for this hypothesis. Therefore, in the TiO_2-Ag_3PO_4 heterojunction system, although the formation of heterojunction optimized the photo-excited electrons and holes transfer, it is not enough to take advantage of the accumulated photo-induced electrons to improve photoactivity and stability of Ag_3PO_4.

In the TiO_2-Ag_3PO_4 heterojunction system, it is necessary to engineer band structures to manipulate a photoinduced charge transfer. It is difficult to modify the Ag_3PO_4 directly due to its unique structure. There have been reports of TiO_2 modification to harvest the sunlight, in which defects production is considered to be one of the most effective modification methods [17]. It has been reported that the defects introduced into photocatalysts can narrow the bandgap to benefit light harvest and also serve as active sites to trap photogenerated electrons and absorb oxygen molecules due to its reduced energy barrier [3,18]. TiO_{2-x}/Ag_3PO_4 has also been reported due to the enhanced photocatalytic degradation of dyes, phenols, and antibiotics [19–21]. In the composite TiO_{2-x}/Ag_3PO_4, the oxygen vacancies on TiO_{2-x} work as activation centers to trap electrons and absorb molecular oxygen to form $\bullet O_2^-$, thus inhibit the recombination of electrons and Ag^+ to form Ag^0 [19], suggesting the promoting effect of oxygen vacancies to form reactive oxygen species. However, the relationship between defects in the photocatalysts and the formation of heterojunction in the hybrid materials has been ignored.

Herein, a novel p-n heterojunction between p-type Ag_3PO_4 and n-type nitrogen-doped black TiO_2 (b-N-TiO_2) was successfully fabricated via the calcination and precipitation method. In the modified TiO_2, the coexistence of incorporated nitrogen and produced oxygen vacancies manipulated the TiO_2 band structure and thus promoted the heterojunction formation in the composite b-N-TiO_2/Ag_3PO_4. The enhanced photocatalytic activity of b-N-TiO_2/Ag_3PO_4 with p-n heterojunction was investigated to degrade harmful algal cells (*Microcystis aeruginosa*) This study aims to fulfill the following objectives: (1) to synthesize and analyze the b-N-TiO_2/Ag_3PO_4 heterojunction system with new properties; (2) to investigate the process of algal cells inactivation by the heterophotocatalyst; (3) to explore the crucial roles of intrinsic defects in the formation of heterojunction and photo-induced charge transfer.

2. Methods and materials

The list of chemicals and algae cultivation methods can be obtained in the Supporting information.

2.1. Photocatalyst preparation

Synthesis of the nitrogen-doped black TiO_2 was reported in our previous work [22]. Briefly, urea (0.6 g) was dispersed into ethanol (20 ml) completely, and then tetrabutyl titanate (14 ml) was added with stirring to form a light-yellow solution; Meanwhile, hydrochloric acid (1 ml), ethanol (10 ml), and deionized water (5 ml) were mixed to form transparent solution, which was then added dropwise to the above light-yellow solution. The formed white colloidal was dried in an oven at 80 °C overnight and then being ground to fine powder, which was calcined under N_2 at 500 °C for 3 h to get black material. The synthesized nitrogen-doped black TiO_2 was designated as b-N-TiO_2. In the process of the b-N-TiO_2/Ag_3PO_4 preparation, different weights of b-N-TiO_2 (0.1, 0.2, or 0.3 g) were dispersed evenly in 100 ml CH_3COOAg solution (3 g/L) using ultrasonication, in which 4 ml of Na_2HPO_4 solution (21.25 g/L) was added dropwise to form b-N-TiO_2/Ag_3PO_4 sediment. The sedimental materials were centrifuged, washed with deionized water and ethanol, and then vacuum dried at 60 °C. The composite samples with various amounts of b-N-TiO_2 were labeled as 0.1T/A, 0.2T/A, and 0.3T/A, in which the weight ratios of b-N-TiO_2 were 28.5%, 44.3%, and 54.4%, respectively. The composite 0.2P25/A was prepared by 0.2 g P25 instead of b-N-TiO_2 using the same method.

2.2. Photocatalytic inactivation of Microcystis aeruginosa

The experiments of photocatalytic inactivation of algal cells (*Microcystis aeruginosa*) were conducted in a reaction box (CEL-LAB500E4, China) with six 120 ml quartz tubes around the Xenon lamp with UV-cutoff filter. The light intensity ($\lambda > 420$ nm) in the position of reaction tubes was kept at 36.7 mW/cm^2. Initial concentrations of algae and photocatalysts in phosphate-buffered saline were approximate 3.0×10^6 cells/ml and 0.2 g/L, respectively. The initial concentration of chlorophyll-a (Chl-a) was 0.85 ± 0.11 mg/L. The volume of the mixture of algal cells and photocatalyst solution was maintained at 100 ml in each reaction tube which was irradiated by visible light with magnetic stirring. Several 5 ml samples were taken to measure the concentrations of Chl-a at predetermined interval times. The Chl-a concentration was calculated according to the method of the report [23]. First, a 5 ml sample was centrifuged for 5 min at 13,000 r/min and removed 4 ml supernatant. Then, ethanol solution (4 ml, 95%, v/v) was added into the precipitate to extract the Chl-a in the algal cells. The ethanol-algae mixture was kept in the refrigerator at 4 °C for 24 h. The optical densities of the extracts were determined with a UV–vis spectrophotometer (UV-1801, BFRL, China) at 649 nm and 665 nm ($A_{649\ nm}$ and $A_{665\ nm}$). The concentrations of Chl-a (C, mg/L) were calculated by $C = 13.7 \times A_{665\ nm} - 5.76 \times A_{649\ nm}$. The schematic diagram of materials synthesization and the experimental process is shown in Fig. S1.

2.3. Analytical methods

The surface morphologies of the photocatalysts and algal cells were obtained by cold-field-emission scanning electron microscopy (FE-SEM, Hitachi S-4800, Japan). The microstructures of photocatalysts were also characterized by transmission electron microscopy (TEM, FEI Tecnai G2 F20 S-Twin, USA). The crystal structures of the photocatalysts were identified by X-ray diffraction (XRD, Bruker D8, Germany) with a Cu-Kα radiation source. X-ray photoelectron spectrometer (XPS) was used to analyze the surface composition of the photocatalysts by PHI-5000C made in the USA. Electron spin resonance (ESR) measurements were conducted on a Bruker E500 spectrometer at room temperature with a microwave power of 1.0 mW and resonance frequency of 9.43 GHz. Raman spectra were recorded using laser excitation at 514 nm with a Horiba LabRAM HR800 Raman Spectrometer. A UV–vis spectrophotometer (Lambda 950, USA) was used to obtain the UV–vis absorbance of the photocatalysts in a range of 200–800 nm. A HORIBA MAX-4 type fluorescence spectrophotometer was used to obtain Photoluminescence spectra (PL). Ultraviolet Photoelectron Spectroscopy (UPS, ESCALAB 250Xi, USA) was conducted using a helium discharge lamp ($h\upsilon = 21.22$ eV) in an ultrahigh vacuum system and a clean Au substrate as reference.

3. Results and discussion

3.1. Morphological and structural characteristics of the photocatalysts

The morphologies of the as-prepared photocatalysts were examined by SEM and TEM. The shapes and sizes of b-N-TiO_2 and 0.2 T/A can be observed in Fig. 1(a) and (b). The shapes of b-N-TiO_2 and 0.2 T/A are

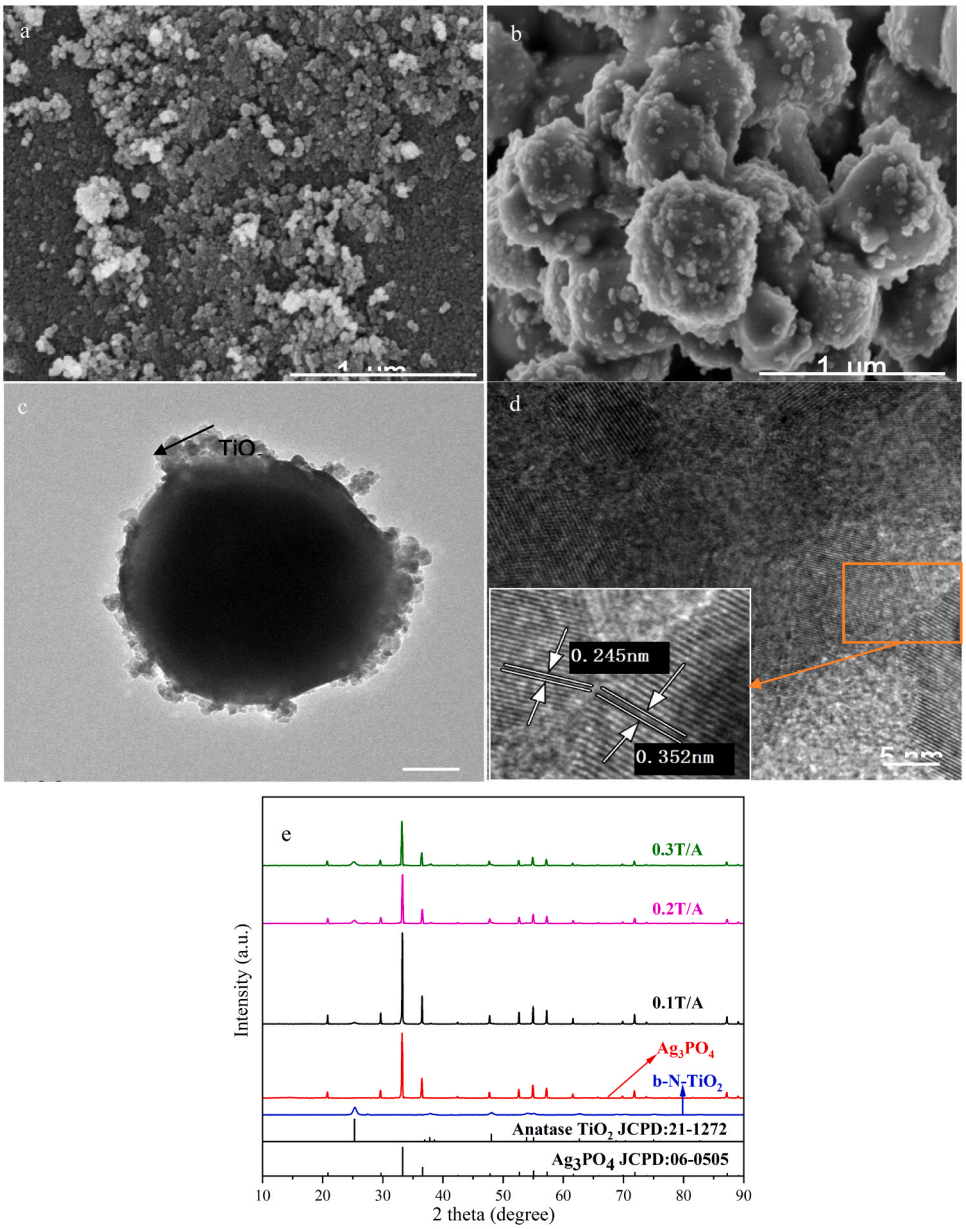

Fig. 1. SEM images of (a) b-N-TiO_2, (b) 0.2T/A; TEM images of (c and d) 0.2T/A; (e) XRD patterns of as-prepared photocatalysts.

both near-spherical. Based on the SEM images, the average particle sizes of b-N-TiO_2 and 0.2 T/A are calculated to be 12.8 ± 3.3 nm and 321.2 ± 145.5 nm (Fig. S2), respectively. According to the particle sizes and morphologies of both materials, it can be investigated that the b-N-TiO_2 particles are evenly distributed over the Ag_3PO_4 particles, which can be identified from the TEM image of 0.2T/A as shown in Fig. 1(c). From the TEM lattice image of 0.2T/A (Fig. 1(d)), the interplanar spacing of 0.352 and 0.245 nm can be indexed to the (101) of TiO_2 and (211) of the Ag_3PO_4, respectively. The combination of b-N-TiO_2 and Ag_3PO_4 can be confirmed by the XRD patterns of 0.1T/A, 0.2T/A, and 0.3T/A as shown in Fig. 1(e). Both of the diffraction peaks of the TiO_2 in the anatase phase (JCPDS No. 21-1272) and the Ag_3PO_4 with the body-centered cubic structure (JCPDS No. 06-0505) existed in all composite materials. As the b-N-TiO_2 content increased, the intensity of diffraction peaks of TiO_2 also increased. During the synthesis, Ag^+ ions were absorbed on the surface of b-N-TiO_2 first, and then the deposited Ag_3PO_4 was formed after the addition of Na_2HPO_4. Although the Ag_3PO_4 should distribute on the surface of b-N-TiO_2 [12], it depends on the particle sizes of both materials [24]. Due to the fast growth of Ag_3PO_4, and thus a much larger size compared with b-N-TiO_2, the composite was b-N-TiO_2-modified Ag_3PO_4 in the present study. Based on the Scherrer formula, the calculated crystal sizes of the Ag_3PO_4 of pure Ag_3PO_4, 0.1T/A, 0.2T/A, and 0.3T/A were 88.58, 104.37, 105.57, and 83.06 nm, respectively, indicating the amount of b-N-TiO_2 affected the crystallization of Ag_3PO_4. The abovementioned observation suggested the successful synthesis of the b-N-TiO_2/Ag_3PO_4 composites and the b-N-TiO_2 attached on the surface of the Ag_3PO_4 well.

The surface states of the as-prepared samples were analyzed by XPS. As shown in Fig. 2(a), the high-resolution Ag 3d spectra peaks in pure Ag_3PO_4 exhibited two peaks at 373.7 and 367.7 eV, attributing to Ag $3d_{3/2}$ and Ag $3d_{5/2}$ of Ag^+, respectively [25]. After the loading of b-N-TiO_2, the binding energy of Ag 3d in 0.2T/A had a low-energy shift by 0.1 eV, indicating the formation of new bonds. Because the electrical negativity of Ti (1.54) is weaker than that of P (2.19) [26], the formation of Ag—O—Ti can be proposed [25]. The formation of Ag—O—Ti covalent interaction was also confirmed by the shift of Ti 2p high-resolution XPS spectra as shown in Fig. 2(b). The XPS peaks of Ti2p in b-N-TiO_2 at 464.3 and 458.2 eV were attributed to Ti $2p_{1/2}$ and Ti $2p_{3/2}$, respectively

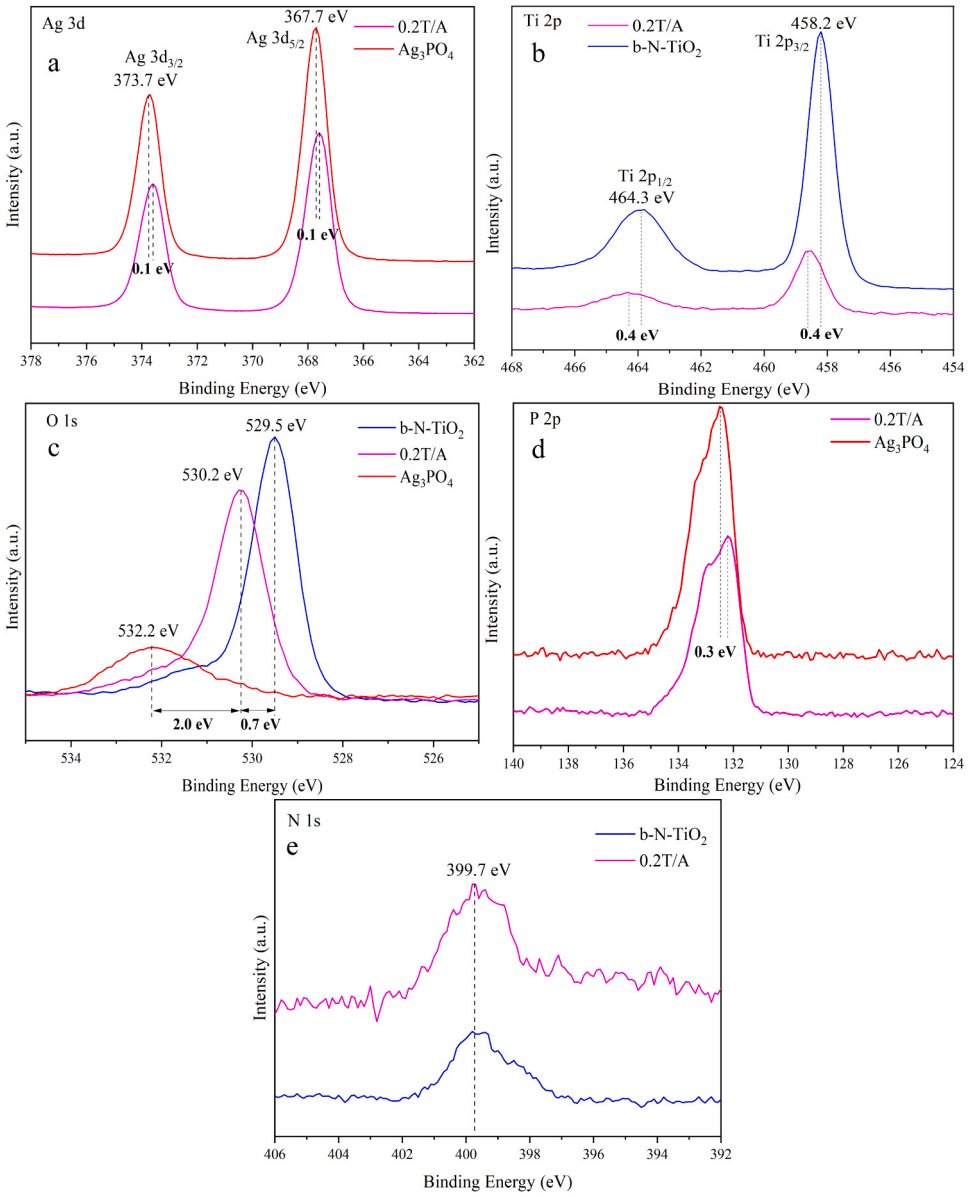

Fig. 2. High-resolution XPS spectra of (a)Ag 3d, (b) Ti 2p, (c) O 1s, (d) P 2p, and (e) N 1s.

[27]. In the 0.2T/A composite, the Ti 2p peaks were broader with a high-energy shift by 0.4 eV, implying the existence of new Ti species with the bond of Ag—O—Ti. The higher-energy shift of Ti in Ag—O—Ti is due to the stronger electrical negativity of Ag (1.93) compared with Ti (1.54). In the O 1s XPS spectra (Fig. 2(c)), the O 1s spectrum of b-N-TiO_2 at 529.5 eV is attributed to lattice oxygen (Ti—O) in TiO_2 [28], and the O 1s spectrum of Ag_3PO_4 at 532.2 eV is related to P—O [11]. Compared with O 1s spectra of b-N-TiO_2 and Ag_3PO_4, the peak of O 1s in composite 0.2T/A occurred a 0.7 eV high-energy shift and a 2.0 eV low-energy shift, respectively, which corresponded to the shift of Ag 3d and Ti 2p, indicating the formation of Ag—O—Ti in the composite. In Fig. 2(d), the P 2p binding energy in the Ag_3PO_4 is 132.5 eV, corresponding to P^{5+} [29]. The P 2p spectrum of composite 0.2T/A occurred a 0.3 eV low-energy shift compared with Ag_3PO_4. P—O—Ag exists in pure Ag_3PO_4, and the P—O—Ti bond probably formed after the b-N-TiO_2 loading in the 0.2T/A composite. The low-energy shift (0.3 eV) of P 2p in the P—O—Ti is due to the weaker electrical negativity of Ti (1.54) compared with Ag (1.93) [30]. The N 1s peak in b-N-TiO_2 [Fig. 2(e)] at 399.7 eV, is contributed to the replacement of lattice oxygen by N atoms to form substitutional N in N—Ti—O [31]. Compared with the N 1s peak in b-N-TiO_2, the N 1s peak in composite 0.2T/A does not occur a significant shift, indicating that the doped N in the b-N-TiO_2 does not affect the combination of b-N-TiO_2 and Ag_3PO_4. In summary, the results of XPS analysis further prove that b-N-TiO_2 and Ag_3PO_4 have been compounded. It was also found that the Ag 3d, P 2p, and O 1s peaks in composite 0.2T/A occurred a low-energy shift compared with pure Ag_3PO_4, while the Ti 2p and O 1s in composite 0.2T/A occurred a high-energy shift compared with b-N-TiO_2. In general, the binding energy has a reverse correlation with the surface electron density [32]. Therefore, the abovementioned results indicate the electrons transfer from b-N-TiO_2 to Ag_3PO_4 in composite 0.2T/A. The interaction between the b-N-TiO_2 and Ag_3PO_4 is beneficial for the formation of the heterojunction and subsequently enhances the photogenerated charge transfer in the composite [33].

N doping and oxygen vacancies formation in b-N-TiO_2 were proven in our previous study [22]. The abovementioned XPS data indicate that the doped N did not change during the synthesis of 0.2T/A. ESR signals represent the defect amount by a paramagnetic spin to indicate the oxygen vacancies in the samples. Fig. 3(a) shows the ESR signals of the b-N-TiO_2, Ag_3PO_4, 0.1T/A, 0.2T/A, and 0.3T/A. The Ag_3PO_4 shows no

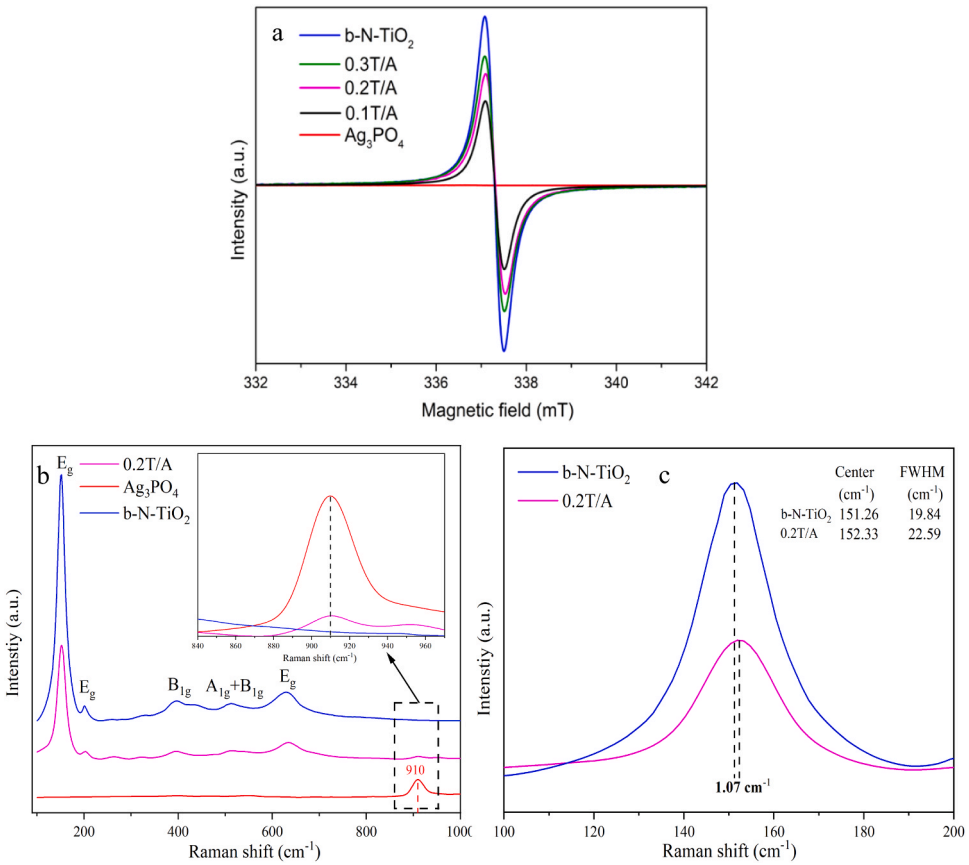

Fig. 3. (a) ESR signals of b-N-TiO_2, Ag_3PO_4, 0.1T/A, 0.2T/A, and 0.3T/A; (b) Raman spectra of b-N-TiO_2, Ag_3PO_4, and 0.2T/A (the inset picture is the enlarged peak at around 910 cm^{-1}); (c) the most intense E_g peak of b-N-TiO_2 and 0.2T/A.

ESR signal, due to it is free of paramagnetic species. The b-N-TiO_2 shows the highest ESR signal, and the intensity decreases with the decreased amount of b-N-TiO_2 in composite 0.3T/A, 0.2T/A, and 0.1T/A. Generally speaking, the ESR peak area is related to the number of oxygen vacancies [34]. It is assumed that the interaction of b-N-TiO_2 and Ag_3PO_4 decreased the content of oxygen vacancies. The calculated g-factor is 1.999 in this research. The g factor close to 2.00 confirms the existence of single electrons trapped by oxygen vacancies [35,36]. The combination of b-N-TiO_2 and Ag_3PO_4 is also confirmed by Raman spectra, as shown in figure (b). The Raman peaks of b-N-TiO_2 locate at 152.57, 201.70, 398.12, 518.31, and 631.22 cm^{-1}, respectively, corresponding to the anatase phase of TiO_2 [37]. The peak shifts from pure TiO_2 to b-N-TiO_2 confirmed oxygen defects caused by the N substitution [38,39]. In the spectrum of the 0.2 T/A composite, the peak around 910 cm^{-1} attributing to the O—P—O vibration confirms the successful introduction of Ag_3PO_4 [40]. Compared with pure b-N-TiO_2, the most evident E_g peak in the 0.2T/A composite occurs a slightly blue shift of 1.07 cm^{-1}, and the full width at half-maximum (FWHM) increases from 19.84 to 22.59 cm^{-1} that was caused by a more serious structural disorder due to the formation of Ag—O—Ti [38,41]. Both the ESR and Raman analyses suggest the existence of covalent bonds on the sample surfaces and oxygen vacancies in the 0.2T/A composite.

3.2. Photoelectric properties

The optical properties of b-N-TiO_2, Ag_3PO_4, and b-N-TiO_2/Ag_3PO_4 composites were shown in Fig. 4(a). Although b-N-TiO_2 has lower absorption compared with pure Ag_3PO_4 and b-N-TiO_2/Ag_3PO_4 in the region of 200–340 nm, the b-N-TiO_2 can harvest full-spectrum visible light. In the region of higher than 466 nm, the composite with coupled b-N-TiO_2 shows higher absorption of visible light than pure Ag_3PO_4. The coupling of b-N-TiO_2 can enhance the harvest of visible light of pure Ag_3PO_4, and the absorption band edges of the composite b-N-TiO_2/Ag_3PO_4 occur red-shift compared with pure Ag_3PO_4. Adsorption intensity of the b-N-TiO_2/Ag_3PO_4 composites is gradually strengthened with increased b-N-TiO_2 loading, indicating the formation of the heterostructure. The optical band gaps of the as-prepared photocatalysts can be estimated from the Tauc plots $((\alpha h\upsilon)^2$ versus $h\upsilon)$ [42] in Fig. 4(b). The E_g values of the samples are 1.45, 1.98, 1.94, 1.92, and 1.80 eV for b-N-TiO_2, Ag_3PO_4, 0.1T/A, 0.2T/A, and 0.3T/A, respectively. After the doping of N and the produced oxygen vacancies, the E_g of b-N-TiO_2 decreases from 3.2 eV [43] to 1.45 eV due to the formed dopant N 2p states and localized defect states [44,45]. The existence of three main emission peaks in the PL spectra at 415, 443, and 467 nm (as shown in Fig. 4(c)) is attributed to the produced oxygen vacancies, indicating the three localized states below the CB minimum in b-N-TiO_2 [46]. As shown in Fig. 4(b) and (c), the coupling of b-N-TiO_2 on the Ag_3PO_4 narrows the E_g of pure Ag_3PO_4 and inhibits the recombination of photogenerated electrons and holes, both of which benefit the photocatalytic performance of the composite.

3.3. Photocatalytic performance and stability of the composite

The photocatalytic performances of the as-prepared photocatalysts were investigated by Chl-a degradation in algal cells of *Microcystis aeruginosa*. As shown in Fig. 5(a), negligible degradation is observed in a blank experiment without any catalyst. With the photocatalyst b-N-TiO_2, 33.0% of the Chl-a is removed in the first hour, however, the concentration of Chl-a does not decrease significantly in the next 7 h. After 8 h of visible light irradiation, the as-prepared photocatalysts b-N-TiO_2, Ag_3PO_4, 0.1T/A, 0.2T/A, 0.2P25/A, and 0.3T/A can achieve 48.4%, 75.0%, 90.3%, 98.1%, 51.3%, and 95.0% of Chl-a removal,

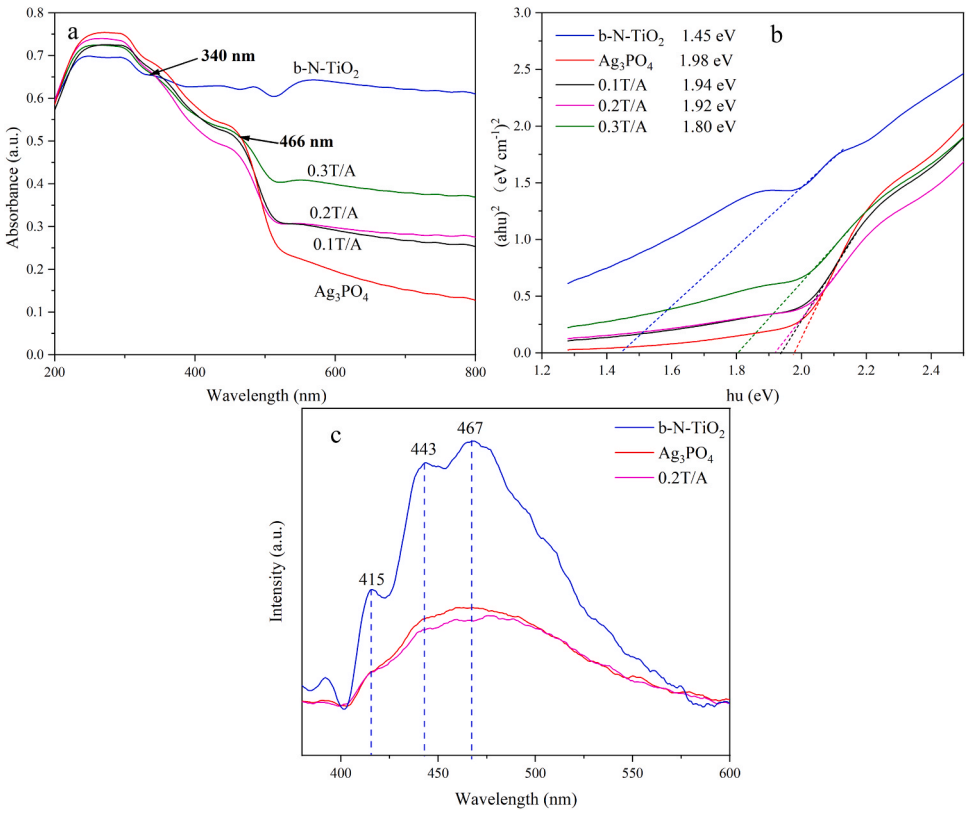

Fig. 4. (a) UV–vis absorption spectra of as-prepared photocatalysts; (b) plots of $(\alpha h\upsilon)^2$ versus the energy of the samples (the intersections of the tangents with the baseline are the sample band gaps); (c) PL spectra of the samples.

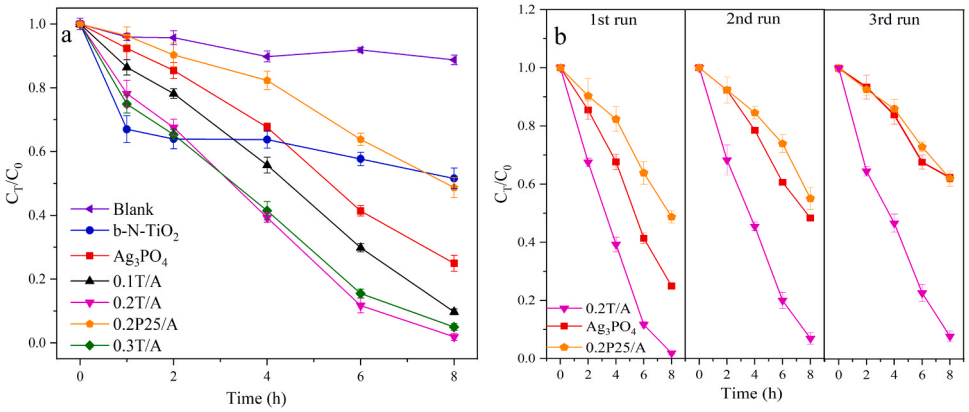

Fig. 5. (a) Photodegradation performance of the as-prepared photocatalysts in degrading Chl-a of algal cells under visible light irradiation; (b) Cycling performance of 0.2T/A, Ag_3PO_4, and 0.2P25/A for of Chl-a degradation.

respectively. The 0.2T/A exhibits the highest photocatalytic degradation of the Chl-a in algal cells. The more b-N-TiO_2 introduction in 0.3T/A decreased the removal rate of the Chl-a. The 0.2P25/A shows less photocatalytic activity than pure Ag_3PO_4, which confirms the important role of b-N-TiO_2 in the composite. Fig. S3 shows the pseudo-first-order dynamics fitting curve of $-\ln(C_t/C_0)$ versus reaction time (C_0 and C_t are the initial concentration and the concentration at time *t*). The pseudo-first-order rate constants (k) are in the high-to-low order of 0.2T/A > 0.3T/A > 0.1T/A > Ag_3PO_4 > 0.2P25/A > b-N-TiO_2 (as shown in Table S1). The 0.2 T/A composite shows the highest kinetic reaction rate (0.4723 h^{-1}), which is 2.7, 7.7, and 6.04 times higher than that of pure Ag_3PO_4 (0.1728 h^{-1}), b-N-TiO_2 (0.0612 h^{-1}), and 0.2P25/A (0.0782 h^{-1}), respectively. The results reveal that the composites b-N-TiO_2/Ag_3PO_4 exhibit better photocatalytic performance than pure Ag_3PO_4, P25/Ag_3PO_4, and b-N-TiO_2. It is well known that it is not stable to apply pure Ag_3PO_4 as the photocatalyst in water [47]. Fig. 5(b) shows the Chl-a degradation efficiency of 0.2 T/A, Ag_3PO_4, and 0.2P25/A after the recycling experiments. The Chl-a removal rate decreases from 75.0% to 37.6% by Ag_3PO_4 after three times recycling experiments, and the Chl-a removal rate of 0.2T/A decreases from 98.1% to 92.1% by 0.2T/A in the three recycling experiments, which demonstrates the stability of the 0.2T/A composite. 0.2P25/A shows less stability than 0.2 T/A, which indicates the difference of b-N-TiO_2 and P25 in the composite. The stability of composite has been contributed to the p-n heterojunction due to the oxygen vacancies and doping N in b-N-TiO_2.

The morphologic changes of algal cells were also investigated. As shown in Fig. 6(a) and (b), the *Microcystis aeruginosa* cells are plump spheres with smooth surfaces after adsorption. After 8 h of visible light

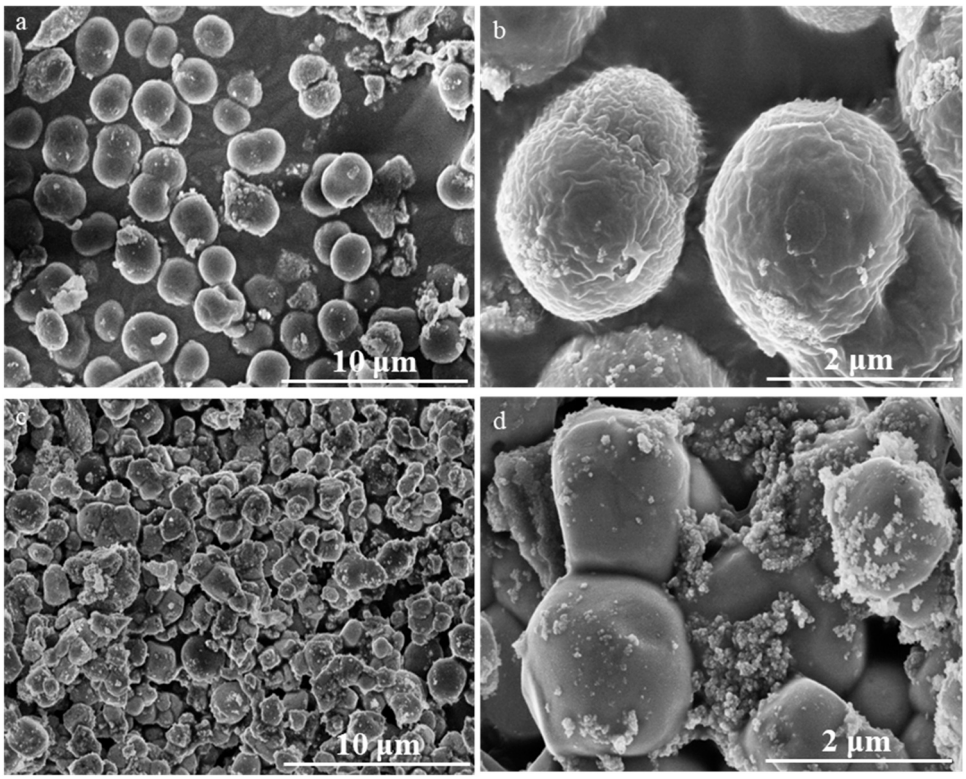

Fig. 6. SEM images of *Microcystis aeruginosa* cells with 0.2 g/L 0.2T/A (a) (b) after adsorption for 2 h, and (c)(d) after irradiation for 8 h under visible light.

irradiation, the morphologies of algal cells changed obviously. The algal cells became deformed and wrinkled [Fig. 6(c) and (d)]. The morphological changes and Chl-a degradation indicate the damages inside algal cells. Based on the Chl-a degradation completely, it can be proposed that the active sites of photocatalyst on algal cells are the chloroplasts inside algal cells. Similar results have been obtained in the previous study [48]. The release of intracellular substances can be confirmed by the changes of components of dissolved organic matters measuring by EEM.

Fig. 7 shows the changes of fluorescence intensity in different regions between the raw surface water [Fig. 7(a)] and the sample after 8 h of sunlight irradiation with 0.2T/A photocatalysts [Fig. 7(b)]. The fluorescence spectrum of raw surface water was divided into four regions for this study including region A with E_x/E_m = (240 – 256)/(330 – 350) representing aromatic protein, region B with E_x/E_m = (274 – 296)/(310 – 350) representing soluble microbial byproduct-like, region C with E_x/E_m = (300 – 340)/(390 – 430) representing humic-like substances, and region D with E_x/E_m = (245 – 265)/(390 – 430) representing fulvic acid-like substances, respectively [49,50]. After 8 h of sunlight irradiation with the 0.2T/A photocatalyst, the fluorescence intensities in regions of A, C, and D decrease significantly, and the intensity in region B increases. This result indicates that the original organic substances including aromatic proteins, the humic-like and fulvic acid-like substances, have been destructed by the photocatalysts. However, the soluble microbial byproduct-like components are released into the water, which suggests a change in biological activity and degradation of the algal cells [51]. The results indicated that the photocatalytic processes of 0.2T/A not only damaged the algal cells but also degraded the organic substances in the surrounding environments.

3.4. Mechanism analysis

The reactive radicals are important for the degradation of pollutants in the photocatalytic processes, which can be analyzed by scavenging experiments and the ESR results. In the scavenging experiment, •OH, $•O_2^-$ and h^+ were consumed by 1 mM isopropanol, benzoquinone, and ethylenediaminetetraacetic acid disodium salt (Na_2-EDTA),

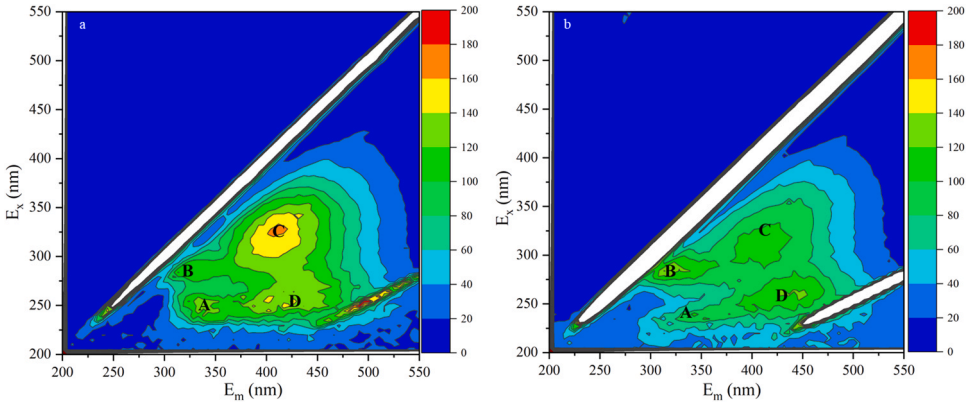

Fig. 7. (a) EEM spectra of dissolved organic matters in the raw surface water; (b) after 8 h sunlight irradiation (at September) with 0.056 g/L 0.2T/A.

respectively. The concentrations of radical scavengers were calculated by the molar ratio [scavenger]: [initial Chl-a] = 1000:1 [52]. As shown in Fig. 8(a), the Chl-a degradation is significantly inhibited when benzoquinone is introduced to the reaction solutions, indicating that $\bullet O_2^-$ is the vital active species for involving in the degradation of Chl-a in algal cells. Furthermore, •OH and h^+ play minor roles for the Chl-a degradation. The ESR results in Fig. 8(b) demonstrate the production of •OH and $\bullet O_2^-$. No ESR signals of DMPO-•OH and DMPO-$\bullet O_2^-$ are observed in dark. There are high DMPO-$\bullet O_2^-$ signals upon visible light irradiation for 1 min, but there is no DMPO-•OH signal appeared in this system. There are only weak DMPO-•OH signals appeared in ESR results even after 5 min visible light irradiation. It confirms the vital role of $\bullet O_2^-$. In our previous study, it was investigated that the dominant ROS in the photocatalytic process of pure Ag_3PO_4 was •OH. Compared with the pure Ag_3PO_4, the composite b-N-TiO_2/Ag_3PO_4 showed different photo-incited charges transfer. As is well known, the generation of $\bullet O_2^-$ is due to the transfer of photo-induced charges and the absorption of oxygen molecules, in which the photogenerated electrons are transferred to the π* orbitals of oxygen molecules to form $\bullet O_2^-$ [3]. Thus, it is crucial to analyze the charge transfer in the photocatalytic process of the b-N-TiO_2/Ag_3PO_4 system.

The band structure of composite is indispensable to explore the photogenerated charge transfer pathways and the p-n heterojunction formation. The UPS is applied to determine the location of the energy band of pure Ag_3PO_4 and b-N-TiO_2 [53]. Fig. 9(a) and (b) show the calculated work functions by the Thermo Scientific Avantage System, which are 8.00 and 5.71 eV for pure Ag_3PO_4 and b-N-TiO_2, respectively. The corresponding Fermi levels (E_F) are then −8.00 and −5.71 eV for pure Ag_3PO_4 and b-N-TiO_2, respectively. The distance between E_F and E_v (the valence band energy) is 0.22 and 1.28 eV for pure Ag_3PO_4 and b-N-TiO_2, respectively [as shown in Fig. 9(a) and (b)]. Therefore, the calculated maximum E_v of pure Ag_3PO_4 and b-N-TiO_2 are −8.22 and −6.99 eV, respectively. The minimum conduction band energy (E_c) of pure Ag_3PO_4 and b-N-TiO_2 is estimated at −6.24 and −5.54 eV according to $E_c = E_v - E_g$. All the abovementioned values are versus the vacuum level. According to the abovementioned calculations, the band structure diagram for b-N-TiO_2 and Ag_3PO_4 is shown in Fig. 9(c). As shown in Fig. 9(c), the band structures of p-type Ag_3PO_4 and n-type b-N-TiO_2 are staggered, and the E_F of b-N-TiO_2 and Ag_3PO_4 are at different levels. Thus, once pure Ag_3PO_4 and b-N-TiO_2 are combined and the p-n junction is created, the difference of E_F between b-N-TiO_2 and Ag_3PO_4 drives the electron flow from b-N-TiO_2 to Ag_3PO_4, and the holes flow in an opposite direction until forming a uniform Fermi level [54]. The electron transfer direction after the two materials are combined is also confirmed by the XPS results (Fig. 2). The band structures of the composite after band equilibrium formation are shown in Fig. 9(d). At the same time, a built-in electric field is formed between b-N-TiO_2 (positively charged region) and Ag_3PO_4 (negatively charged region). When the b-N-TiO_2/Ag_3PO_4 composite is exposed to visible light, the photogenerated charges could be effectively transferred because of the built-in electric potential in the p-n heterojunction. As shown in Fig. 9 (d), the photo-induced holes in the VB of b-N-TiO_2 transfer to the VB of the Ag_3PO_4, and then the holes can be consumed to oxide OH^-/H_2O_2 to form •OH or damage algal cells directly. What is the transfer pathway of photogenerated electrons in the composite? From our previous publication focusing on b-N-TiO_2, we know that the oxygen vacancies (O_v) and doping N existing in b-N-TiO_2 could form localized states (Ti^{3+}+O_v) and N 2p states to narrow the bandgap [22,55–57]. Thus, the electrons in the VB of b-N-TiO_2 and local N 2p states are excited to the defect states upon visible light irradiation. On the other hand, the photo-induced electrons in the CB of the Ag_3PO_4 can be transferred to the defect states of the b-N-TiO_2 due to the built-in electric potential, which inhibited the reduction of Ag^+ to Ag^0 in Ag_3PO_4. Furthermore, the oxygen vacancies near the CB of the b-N-TiO_2 can act as an absorption active center of oxygen molecules for consuming the electrons [19], which can improve the reduction of O_2 to $\bullet^* O_2^-$ (in a chemisorbed state) [3,58] and participation in the subsequent oxidation processes. In conclusion, the induced defects and doping N 2p in b-N-TiO_2 could narrow the bandgap and then facilitate the formation of p-n heterojunction between b-N-TiO_2 and Ag_3PO_4. On one hand, the electrons from CB of Ag_3PO_4 were trapped by the existing oxygen vacancies, which inhibited the corrosion of Ag_3PO_4 and then improved the stability of composite b-N-TiO_2/Ag_3PO_4. On the other hand, the induced defects improved the utilization of absorbed molecular oxygen and electrons to form more oxide radicals, thus enhanced the photocatalytic activities of composite b-N-TiO_2/Ag_3PO_4 for degrading algal cells.

4. Conclusion

In summary, the p-n heterojunction in the novel b-N-TiO_2/Ag_3PO_4 composite was successfully fabricated via the calcination and precipitation method. The incorporated nitrogen and produced oxygen vacancies narrowed the bandgap and shifted the band position of TiO_2, which facilitated the formation of p-n heterojunction in the b-N-TiO_2/Ag_3PO_4 composite and then increased the separation and transfer efficiencies of photo-induced electrons and holes. The introduction of b-N-TiO_2 not only increased the harvest of visible light but also decreased the recombination of photogenerated electrons and holes. As a result, the b-N-TiO_2/Ag_3PO_4 exhibited enhanced photocatalytic activity for algal cell degradation which was 2.73, 7.72, and 6.04 times higher than that of the pure Ag_3PO_4, b-N-TiO_2, and P25/Ag_3PO_4, respectively. Finally, the mechanism of enhanced photocatalytic performance due to p-n

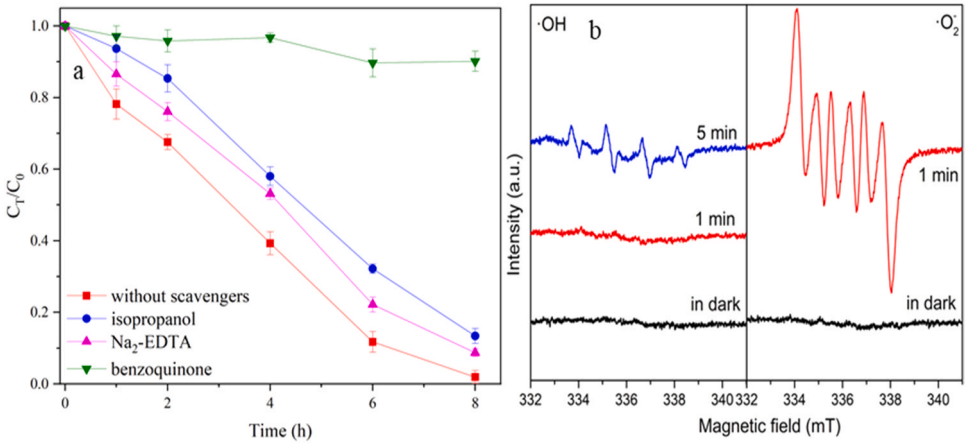

Fig. 8. (a) Photocatalytic degradation of Chl-a with additions of various scavengers over composite 0.2T/A, and (b) ESR results of DMPO-•OH (in aqueous solution) and DMPO-$\bullet O_2^-$ (in methanol solution) over 0.2T/A.

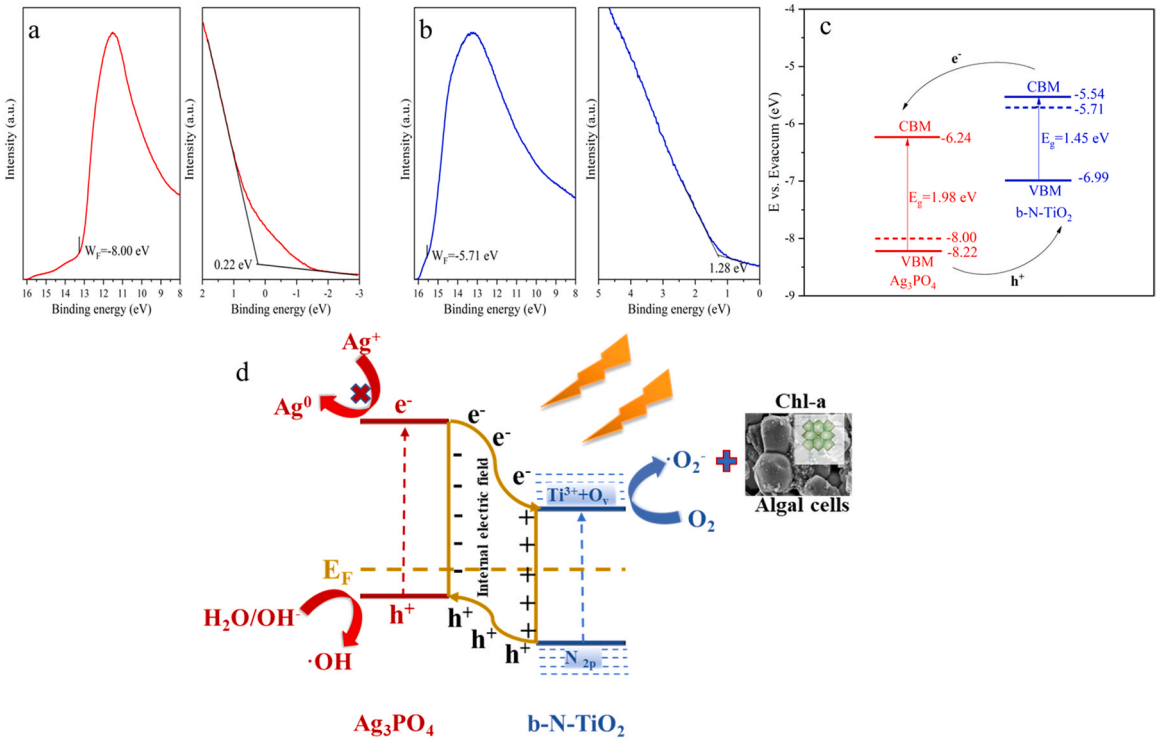

Fig. 9. UPS spectra of (a) Ag_3PO_4 and (b) b-N-TiO_2; (c) band structure diagram for Ag_3PO_4 and b-N-TiO_2 before band equilibrium; (d) proposed photocatalytic mechanism for the composite b-N-TiO_2/Ag_3PO_4.

heterojunction in the composite has been proposed based on the relative band positions and Fermi levels of these two semiconductors. In the degradation process, the $\bullet O_2^-$ was the dominant reactive radical to degrade the algal cells. Overall, the photocatalyst in this study has potential application for harmful algae polluted water treatment in the future.

CRediT authorship contribution statement

Li Zhou: Investigation, Validation, Funding acquisition, Data curation, Writing – original draft. **Xu Zhang:** Methodology, Formal analysis, Funding acquisition. **Min Cai:** Formal analysis, Resources. **Naxin Cui:** Data curation. **Guifa Chen:** Validation, Resources. **Guoyan Zou:** Conceptualization, Project administration, Writing – review & editing.

Declaration of Competing Interest

The authors declare that they have no known competing financial interests or personal relationships that could have appeared to influence the work reported in this paper.

Acknowledgments

This research was financially supported by the Natural Science Foundation of Shanghai (21ZR1456700), the Shanghai Sailing Program (21YF1440900), and the National Natural Science Foundation of China (No. 42007147).

Appendix A. Supporting information

Supplementary data associated with this article can be found in the online version at doi:10.1016/j.apcatb.2021.120868.

References

[1] M. Le Moal, C. Gascuel-Odoux, A. Ménesguen, Y. Souchon, C. Étrillard, A. Levain, F. Moatar, A. Pannard, P. Souchu, A. Lefebvre, G. Pinay, Eutrophication: a new wine in an old bottle? Sci. Total Environ. 651 (2019) 1–11.
[2] K.J. Iwinski, J.H. Rodgers, C.M. Kinley, M. Hendrikse, A.J. Calomeni, A. D. McQueen, T.D. Geer, J. Liang, V. Friesen, M. Haakensen, Influence of $CuSO_4$ and chelated copper algaecide exposures on biodegradation of microcystin-LR, Chemosphere 174 (2017) 538–544.
[3] L. Xiong, J. Tang, Strategies and challenges on selectivity of photocatalytic oxidation of organic substances, Adv. Energy Mater. 11 (2021) 1–19.
[4] X. Wang, X. Wang, J. Zhao, J. Song, L. Zhou, R. Ma, J. Wang, X. Tong, Y. Chen, Efficient visible light-driven in situ photocatalytic destruction of harmful alga by worm-like N,P co-doped TiO_2/expanded graphite carbon layer (NPT-EGC) floating composites, Catal. Sci. Technol. 7 (2017) 2335–2346.
[5] Z. Diao, S. Pu, W. Qian, S. Liang, L. Kong, D. Xia, Z. Lei, J. Du, H. Liu, J. Yang, Photocatalytic removal of phenanthrene and algae by a novel Ca-Ag_3PO_4 composite under visible light: reactivity and coexisting effect, Chemosphere 221 (2019) 511–518.
[6] P. Dong, Y. Wang, B. Cao, S. Xin, L. Guo, J. Zhang, F. Li, Ag_3PO_4/reduced graphite oxide sheets nanocomposites with highly enhanced visible light photocatalytic activity and stability, Appl. Catal. B Environ. 132–133 (2013) 45–53.
[7] H. Wang, Y. Bai, J. Yang, X. Lang, J. Li, L. Guo, A facile way to rejuvenate Ag_3PO_4 as a recyclable highly efficient photocatalyst, Chem. Eur. J. 18 (2012) 5524–5529.
[8] C. Tang, E. Liu, J. Wan, X. Hu, J. Fan, Co_3O_4 nanoparticles decorated Ag_3PO_4 tetrapods as an efficient visible-light-driven heterojunction photocatalyst, Appl. Catal. B Environ. 181 (2016) 707–715.
[9] V. Rodríguez-González, S. Obregón, O.A. Patrón-Soberano, C. Terashima, A. Fujishima, An approach to the photocatalytic mechanism in the TiO_2-nanomaterials microorganism interface for the control of infectious processes, Appl. Catal. B Environ. 270 (2020), 118853.
[10] Z. Yi, J. Ye, N. Kikugawa, T. Kako, S. Ouyang, H. Stuart-Williams, H. Yang, J. Cao, W. Luo, Z. Li, Y. Liu, R.L. Withers, An orthophosphate semiconductor with photooxidation properties under visible-light irradiation, Nat. Mater. 9 (2010) 559–564.
[11] Y. Li, L. Yu, N. Li, W. Yan, X. Li, Heterostructures of Ag_3PO_4/TiO_2 mesoporous spheres with highly efficient visible light photocatalytic activity, J. Colloid Interface Sci. 450 (2015) 246–253.
[12] W. Yao, B. Zhang, C. Huang, C. Ma, X. Song, Q. Xu, Synthesis and characterization of high efficiency and stable Ag_3PO_4/TiO_2 visible light photocatalyst for the degradation of methylene blue and rhodamine B solutions, J. Mater. Chem. 22 (2012) 4050–4055.
[13] S.B. Rawal, S.D. Sung, W.I. Lee, Novel Ag_3PO_4/TiO_2 composites for efficient decomposition of gaseous 2-propanol under visible-light irradiation, Catal. Commun. 17 (2012) 131–135.

[14] L. Cai, Q. Long, C. Yin, Synthesis and characterization of high photocatalytic activity and stable Ag_3PO_4/TiO_2 fibers for photocatalytic degradation of black liquor, Appl. Surf. Sci. 319 (2014) 60–67.

[15] B. Liu, Y. Xue, J. Zhang, B. Han, J. Zhang, X. Suo, L. Mu, H. Shi, Visible-light-driven TiO_2/Ag_3PO_4 heterostructures with enhanced antifungal activity against agricultural pathogenic fungi Fusarium graminearum and mechanism insight, Environ. Sci. Nano 4 (2017) 255–264.

[16] C. Liu, T. Perng, Fabrication and band structure of Ag_3PO_4–TiO_2 heterojunction with enhanced photocatalytic hydrogen evolution, Int. J. Hydrog. Energy 45 (2020) 149–159.

[17] S.A.A. Anaam, H. Saim, M.Z. Sahdan, A. Al-Gheethi, Defective TiO_2 with intrinsic point defects for photocatalytic hydrogen production: a review, Int. J. Nanoelectron. Mater. 12 (2019) 495–514.

[18] N. Zhang, X.Y. Li, H.C. Ye, S.M. Chen, H.X. Ju, D.B. Liu, Y. Lin, W. Ye, C.M. Wang, Q. Xu, J.F. Zhu, L. Song, J. Jiang, Y.J. Xiong, Oxide defect engineering enables to couple solar energy into oxygen activation, J. Am. Chem. Soc. 138 (2016) 8928–8935.

[19] J.X. Liu, F.X. Xie, R. Li, T. Li, Z.H. Jia, Y.F. Wang, Y.W. Wang, X.C. Zhang, C. M. Fan, TiO_{2-X}/Ag_3PO_4 photocatalyst: oxygen vacancy dependent visible light photocatalytic performance and BPA degradative pathway, Mater. Sci. Semicond. Process. 97 (2019) 1–10.

[20] Q. Guan, S. Khan, Z. Wang, Q. Liu, L. Zhang, Y. Zhao, X. Wang, X. Yang, Z. Geng, The preparation, characterization of TiO_{2-X}/Ag_3PO_4 heterojunctions with enhanced photocatalytic visible-light performance, J. Alloy. Compd. 852 (2021), 156947.

[21] Y. Wang, H. Yu, Y. Lu, J. Qu, S. Zhu, M. Huo, A nano-composite comprised of Ti^{3+}-doped TiO_2 nanotubes and Ag_3PO_4 quantum dots with enhanced photocatalytic activity under visible light, Mater. Lett. 240 (2019) 35–38.

[22] L. Zhou, M. Cai, X. Zhang, N. Cui, G. Chen, G.-y Zou, In-situ nitrogen-doped black TiO_2 with enhanced visible-light-driven photocatalytic inactivation of *Microcystis aeruginosa* cells: synthesization, performance and mechanism, Appl. Catal. B Environ. 272 (2020), 119019.

[23] H.K. Lichtenthaler, A.R. Wellburn, Determinations of total carotenoids and chlorophylls *a* and *b* of leaf extracts in different solvents, Biochem. Soc. Trans. 11 (1983) 591–592.

[24] F. Zhao, L. Pan, S. Wang, Q. Deng, J. Zou, L. Wang, X. Zhang, Ag_3PO_4/TiO_2 composite for efficient photodegradation of organic pollutants under visible light, Appl. Surf. Sci. 317 (2014) 833–838.

[25] Z.W. Tong, D. Yang, Y.Y. Sun, Y. Tian, Z.Y. Jiang, In situ fabrication of Ag_3PO_4/TiO_2 nanotube heterojunctions with enhanced visible-light photocatalytic activity, Phys. Chem. Chem. Phys. 17 (2015) 12199–12206.

[26] L. Ma, H. Han, L. Pan, M. Tahir, L. Wang, X.W. Zhang, J.J. Zou, Fabrication of TiO_2 nanosheets via Ti^{3+} doping and Ag_3PO_4 QD sensitization for highly efficient visible-light photocatalysis, RSC Adv. 6 (2016) 63984–63990.

[27] W. Liu, H. Zhang, H. Wang, M. Zhang, M. Guo, Titanium mesh supported TiO_2 nanowire arrays/upconversion luminescence Er^{3+}-Yb^{3+} codoped TiO_2 nanoparticles novel composites for flexible dye-sensitized solar cells, Appl. Surf. Sci. 422 (2017) 304–315.

[28] A. Naldoni, M. Allieta, S. Santangelo, M. Marelli, F. Fabbri, S. Cappelli, C. L. Bianchi, R. Psaro, V. Dal Santo, Effect of nature and location of defects on bandgap narrowing in black TiO_2 nanoparticles, J. Am. Chem. Soc. 134 (2012) 7600–7603.

[29] R. Zheng, L. Lin, J. Xie, Y. Zhu, Y. Me, State of doped phosphorus and its influence on the physicochemical and photocatalytic properties of P-doped titania, J. Phys. Chem. C 112 (2008) 15502–15509.

[30] A.N. Martín-Gómez, J.A. Navío, C. Jaramillo-Páez, P. Sánchez-Cid, M.C. Hidalgo, Hybrid ZnO/Ag_3PO_4 photocatalysts, with low and high phosphate molar percentages, J. Photochem. Photobio. A Chem. 388 (2020), 112196.

[31] X. Yan, Z. Xing, Y. Cao, M. Hu, Z. Li, X. Wu, Q. Zhu, S. Yang, W. Zhou, In-situ C-N-S-tridoped single crystal black TiO_2 nanosheets with exposed {001} facets as efficient visible-light-driven photocatalysts, Appl. Catal. B Environ. 219 (2017) 572–579.

[32] Y. Zhuang, H. Tan, Y. Liu, Y. Zhang, Y. Ling, High resolution visualization of Görtler-like vortices in supersonic compression ramp flow, J. Vis. 20 (2017) 505–508.

[33] C.S. Pan, J. Xu, Y.J. Wang, D. Li, Y.F. Zhu, Dramatic activity of $C_3N_4/BiPO_4$ photocatalyst with core/shell structure formed by self-assembly, Adv. Funct. Mater. 22 (2012) 1518–1524.

[34] Y. Wu, S. Chen, J. Zhao, X. Yue, W. Deng, Y. Li, C. Wang, Mesoporous graphitic carbon nitride and carbon–TiO_2 hybrid composite photocatalysts with enhanced photocatalytic activity under visible light irradiation, J. Environ. Chem. Eng. 4 (2016) 797–807.

[35] S. Zhang, W. Li, Z. Jin, J. Yang, J. Zhang, Z. Du, Z. Zhang, Study on ESR and inter-related properties of vacuum-dehydrated nanotubed titanic acid, J. Solid State Chem. 177 (2004) 1365–1371.

[36] Z.A. Lin, W.C. Lu, C.Y. Wu, K.S. Chang, Facile fabrication and tuning of TiO_2 nanoarchitectured morphology using magnetron sputtering and its applications to photocatalysis, Ceram. Int. 40 (2014) 15523–15529.

[37] W. Zhou, F. Sun, K. Pan, G. Tian, B. Jiang, Z. Ren, C. Tian, H. Fu, Well-ordered large-pore mesoporous anatase TiO_2 with remarkably high thermal stability and improved crystallinity: preparation, characterization, and photocatalytic performance, Adv. Funct. Mater. 21 (2011) 1922–1930.

[38] X. Chen, L. Liu, P.Y. Yu, S.S. Mao, Increasing solar absorption for photocatalysis with black hydrogenated titanium dioxide nanocrystals, Science 331 (2011) 746–750.

[39] X. Zhang, M. Cai, N. Cui, G. Chen, G. Zou, L. Zhou, One-step synthesis of b-N-TiO_2/C nanocomposites with high visible light photocatalytic activity to degrade *Microcystis aeruginosa*, Catalysts 10 (2020), 579.

[40] M. Batvandi, A. Haghighatzadeh, B. Mazinani, Synthesis of Ag_3PO_4 microstructures with morphology-dependent optical and photocatalytic behaviors, Appl. Phys. A Mater. Sci. Process. 126 (2020) 16.

[41] X. Liu, Z. Xing, H. Zhang, W. Wang, Y. Zhang, Z. Li, X. Wu, X. Yu, W. Zhou, Fabrication of 3 D mesoporous black $TiO_2/MoS_2/TiO_2$ nanosheets for visible-light-driven photocatalysis, ChemSusChem 9 (2016) 1118–1124.

[42] J. Nie, G. Zhu, W. Zhang, J. Gao, P. Zhong, X. Xie, Y. Huang, M. Hojamberdiev, Oxygen vacancy defects-boosted deep oxidation of NO by β-$Bi_2O_3/CeO_{2-\delta}$ p-n heterojunction photocatalyst in situ synthesized from $Bi/Ce(CO_3)(OH)$ precursor, Chem. Eng. J. 424 (2021), 130327.

[43] R. Pandiyan, N. Delegan, A. Dirany, P. Drogui, M.A. El Khakani, Probing the electronic surface properties and bandgap narrowing of in situ N, W, and (W,N) doped magnetron-sputtered TiO_2 films intended for electro-photocatalytic applications, J. Phys. Chem. C 120 (2016) 631–638.

[44] F. Zuo, L. Wang, T. Wu, Z. Zhang, D. Borchardt, P. Feng, Self-doped Ti^{3+} enhanced photocatalyst for hydrogen production under visible light, J. Am. Chem. Soc. 132 (2010) 11856–11857.

[45] A.K. Rumaiz, J.C. Woicik, E. Cockayne, H.Y. Lin, G.H. Jaffari, S.I. Shah, Oxygen vacancies in N doped anatase TiO_2: experiment and first-principles calculations, Appl. Phys. Lett. 95 (2009), 262111.

[46] Q. Hu, G. Li, H. Lan, J. Li, B. Hu, W. Guo, J. Huang, X. Huang, Facile coengineering of oxygen defects and highly active {110} facets in TiO_2 nanorods for efficient water splitting, Cryst. Growth Des. 19 (2019) 1680–1688.

[47] L. Zhou, O.G. Alvarez, C.S. Mazon, L. Chen, M. Sui, The roles of conjugations of graphene and Ag in Ag_3PO_4-based photocatalysts for degradation of sulfamethoxazole, Catal. Sci. Technol. 6 (2016) 5972–5981.

[48] F.M. Li, Z. Liang, X. Zheng, W. Zhao, M. Wu, Z.Y. Wang, Toxicity of nano-TiO_2 on algae and the site of reactive oxygen species production, Aquat. Toxicol. 158 (2015) 1–13.

[49] W. Chen, P. Westerhoff, J. Leenheer, K. Booksh, Fluorescence excitation-emission matrix regional integration to quantify spectra for dissolved organic matter, Environ. Sci. Technol. 37 (2003) 5701–5710.

[50] M. Ziegmann, M. Abert, M. Müller, F.H. Frimmel, Use of fluorescence fingerprints for the estimation of bloom formation and toxin production of *Microcystis aeruginosa*, Water Res. 44 (2010) 195–204.

[51] S. Determann, J.M. Lobbes, R. Reuter, J. Rullkotter, Ultraviolet fluorescence excitation and emission spectroscopy of marine algae and bacteria, Mar. Chem. 62 (1998) 137–156.

[52] S. Nasseri, A.H. Mahvi, M. Seyedsalehi, K. Yaghmaeian, R. Nabizadeh, M. Alimohammadi, G.H. Safari, Degradation kinetics of tetracycline in aqueous solutions using peroxydisulfate activated by ultrasound irradiation: effect of radical scavenger and water matrix, J. Mol. Liq. 241 (2017) 704–714.

[53] J. Liu, Y. Liu, N. Liu, Y. Han, X. Zhang, H. Huang, Y. Lifshitz, S.-T. Lee, J. Zhong, Z. Kang, Metal-free efficient photocatalyst for stable visible water splitting via a two-electron pathway, Science 347 (2015) 970–974.

[54] T. Cai, L. Wang, Y. Liu, S. Zhang, W. Dong, H. Chen, X. Yi, J. Yuan, X. Xia, C. Liu, S. Luo, Ag_3PO_4/Ti_3C_2 MXene interface materials as a Schottky catalyst with enhanced photocatalytic activities and anti-photocorrosion performance, Appl. Catal. B Environ. 239 (2018) 545–554.

[55] Y. Lei, L.D. Zhang, G.W. Meng, G.H. Li, X.Y. Zhang, C.H. Liang, W. Chen, S. X. Wang, Preparation and photoluminescence of highly ordered TiO_2 nanowire arrays, Appl. Phys. Lett. 78 (2001) 1125–1127.

[56] L. Jing, Y. Qu, B. Wang, S. Li, B. Jiang, L. Yang, W. Fu, H. Fu, Review of photoluminescence performance of nano-sized semiconductor materials and its relationships with photocatalytic activity, Sol. Energy Mater. Sol. Cells 90 (2006) 1773–1787.

[57] S. Hoang, S.P. Berglund, N.T. Hahn, A.J. Bard, C.B. Mullins, Enhancing visible light photo-oxidation of water with TiO_2 nanowire arrays via cotreatment with H_2 and NH_3: synergistic effects between Ti^{3+} and N, J. Am. Chem. Soc. 134 (2012) 3659–3662.

[58] N. Zhang, X. Li, H. Ye, S. Chen, H. Ju, D. Liu, Y. Lin, W. Ye, C. Wang, Q. Xu, J. Zhu, L. Song, J. Jiang, Y. Xiong, Oxide defect engineering enables to couple solar energy into oxygen activation, J. Am. Chem. Soc. 138 (2016) 8928–8935.